ISSN: 2160-049X Volume 9, Number 12, December 2019

Scientific Research Publishing

World Journal of Mechanics

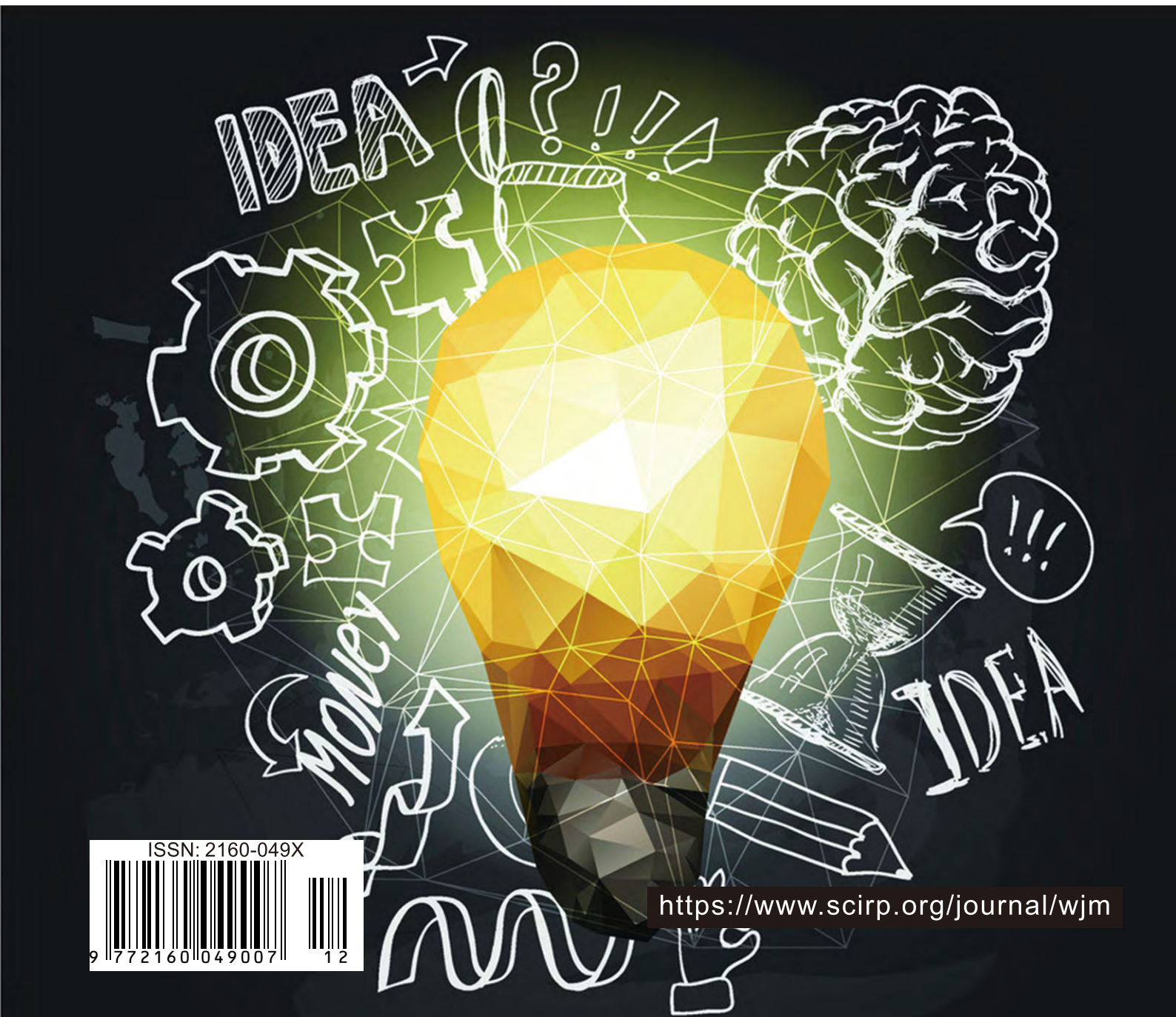

ISSN: 2160-049X
9 772160 049007 12

https://www.scirp.org/journal/wjm

Journal Editorial Board

ISSN 2160-049X (Print) ISSN 2160-0503 (Online)

https://www.scirp.org/journal/wjm

Editors-in-Chief

Scientific Research Publishing

World Journal of Mechanics, 2019, 9, 259-284
https://www.scirp.org/journal/wjm
ISSN Online: 2160-0503
ISSN Print: 2160-049X

Table of Contents

Volume 9 Number 12 December 2019

World Journal of Mechanics (WJM)
Journal Information

SUBSCRIPTIONS

The *World Journal of Mechanics* (Online at Scientific Research Publishing, https://www.scirp.org/) is published monthly by Scientific Research Publishing, Inc., USA.

Subscription rates:
Print: $69 per issue.
To subscribe, please contact Journals Subscriptions Department, E-mail: sub@scirp.org

SERVICES

Advertisements
Advertisement Sales Department, E-mail: service@scirp.org

Reprints (minimum quantity 100 copies)
Reprints Co-ordinator, Scientific Research Publishing, Inc., USA.
E-mail: sub@scirp.org

COPYRIGHT

PRODUCTION INFORMATION

For manuscripts that have been accepted for publication, please contact:
E-mail: wjm@scirp.org

World Journal of Mechanics, 2019, 9, 259-266
https://www.scirp.org/journal/wjm
ISSN Online: 2160-0503
ISSN Print: 2160-049X

High Resolution Compact Finite Difference Schemes for Convection Dominated Problems

Abdullah Shah, Saher Akmal Khan, Najib Ullah

Department of Mathematics, COMSATS University Islamabad, Islamabad, Pakistan
Email: abdullah_shah@comsats.edu.pk

How to cite this paper: Shah, A., Khan, S.A. and Ullah, N. (2019) High Resolution Compact Finite Difference Schemes for Convection Dominated Problems. *World Journal of Mechanics*, **9**, 259-266.
https://doi.org/10.4236/wjm.2019.912017

Received: October 21, 2019
Accepted: November 29, 2019
Published: December 2, 2019

Abstract

In this short article, the upwind and central compact finite difference schemes for spatial discretization of the first-order derivative are analyzed. Comparison of the schemes is provided and the best discretization scheme for convection dominated problems is suggested.

Keywords

Upwind Scheme, Upwind Compact Scheme, Flux-Difference Splitting, Convection Dominated Problems

1. Introduction

With the ever-increasing interest in numerical calculations demanding high accuracy for a wide range of length scales, such as large-eddy simulation and direct numerical simulation of turbulence, high-order numerical methods are desired. Particularly, high-order finite difference, finite volume, and finite element methods have received more attention in handling complex problems. These high-order methods try to achieve high accuracy and avoid spurious oscillations and are usually characterized by their self-adaptive nature. The use of high-order methods is particularly warranted by the need to simulate flows containing discontinuous phenomena, such as fluid interfaces and steep shear layers. The compact high-order finite difference schemes provide an effective way of combining the robustness of finite difference schemes and the accuracy of spectral methods [1] [2] [3]. Generally, the computation of derivatives in compact finite differences is implicit in the sense that the derivative values at a particular node are computed not only from the function values but also from the values of the derivative at the neighboring nodes [4]. Compared to non-compact counterparts of the same order of accuracy, compact schemes utilize a smaller stencil, have

smaller truncating errors, and give better resolution especially at higher wave numbers [5] [6]. Compact finite difference schemes can generally be classified into two broad categories: upwind and central. The upwind compact schemes inherently possess the needed dissipation to control the numerical instabilities. Fu and Ma [7] have developed some upwind compact schemes which are successfully implemented by Shah *et al.* [8] [9] [10] [11] for solving fluid flow problems. As these schemes possess appropriate dissipation to prevent non-physical oscillations, they seem to be suitable for solving the convection dominated problems. N.B. Ali *et al.* [12] used implicit and explicit third and fifth-order upwind compact schemes for solving the level set equation. De V. E. and Eswaran, V. [13] have studied some optimized upwind and upwind compact schemes for the solution of acoustic wave problem. Central compact schemes have the advantage of achieving high-order accuracy with fewer grid points in the stencil, but they are non-dissipative, and using central compact schemes on non-staggered meshes for convection terms might cause numerical oscillations even for flows without discontinuities. Reducing or removing such oscillations requires the introduction of dissipation terms or the use of filtering approach [14]. Resolution characteristics imply how compact finite difference approximation represents the exact result over the full range of length scales that can be realized for a given mesh [15]. This work aims to study different compact schemes to find the scheme more suitable for solving convection dominated problems.

2. Model Problem

In order to examine approximating behaviors of various numerical schemes, the following linear convection equation (also known as one-way wave equation) is considered.

$$\frac{\partial u}{\partial t}+c\frac{\partial u}{\partial x}=0,\quad c>0. \tag{1}$$

The semi discrete form Equation (1) is

$$\frac{\partial u_j}{\partial t}+c\frac{\partial u_j}{\partial x_j}=0. \tag{2}$$

The solution of Equation (1) represented by $u(x,t)$ by a typical Fourier mode is given by:

$$u(x,t)=\hat{u}_k(t)\mathrm{e}^{ikx}, \tag{3}$$

$\hat{u}_k$ is the Fourier mode of the wave number k and $i=\sqrt{-1}$, the exact spatial differentiation of Equation (3) is represented by;

$$u'=i(kh)\frac{\hat{u}_k}{h}\mathrm{e}^{ikx}, \tag{4}$$

where the wave number is scaled by the grid size $h=\frac{l}{n}$, where l is the length of domain and n is the number of grids. By analogy the numerical approximation of the derivative is written as [13]

$$u' = k_{eq}(kh)\frac{\hat{u}_k}{h}e^{ikx} = \left(k_r(kh) + i(k_i)kh\right)\frac{\hat{u}_k}{h}e^{ikx}. \tag{5}$$

The exact solution of Equation (1) is $u(x,t) = e^{ik(x-ct)}$, and the exact solution of Equation (2) can be written as $u(x_j,t) = e^{-k_r\frac{ct}{\Delta x}}e^{ik\left(x_j - \frac{k_i}{k\Delta x}ct\right)}$, where the modified wave number $k_{eq} = k_r + ik_i$. k_i is related to the phase speed in the numerical solution, and k_r is related to the numerical damping of a difference scheme. Fourier analysis of different discretization schemes allows us to choose the best scheme.

2.1. Upwind Compact Scheme

In this subsection, third and fifth-order upwind compact and upwind explicit schemes are analyzed. For the third-order upwind compact scheme [16], we have

$$\frac{2}{3}u_j + \frac{1}{3}u_{j-1} = \frac{u_{j+1} + 4u_j - 5u_{j-1}}{6}, \tag{6}$$

that satisfy the relation

$$\begin{aligned} u_j &= \frac{\frac{1}{6}e^{i\alpha} + \frac{2}{3} - \frac{5}{6}e^{-i\alpha}}{\frac{2}{3} + \frac{1}{3}e^{-i\alpha}}\hat{u}(t)e^{ikx_j} \\ &= \frac{\cos\alpha + i\sin\alpha + 4 - 5(\cos\alpha - i\sin\alpha)}{4 + 2(\cos\alpha - i\sin\alpha)}\hat{u}(t)e^{ikx_j} \\ &= \frac{(1-\cos\alpha)^2 + i\sin\alpha(8+\cos\alpha)}{5 + 4\cos\alpha}\hat{u}(t)e^{ikx_j} \end{aligned} \tag{7}$$

where

$$k_r = \frac{(1-\cos\alpha)^2}{5+4\cos\alpha}, \quad k_i = \frac{\sin\alpha(8+\cos\alpha)}{5+4\cos\alpha}. \tag{8}$$

Similarly, for the fifth-order upwind compact scheme [7], we have

$$\frac{3}{5}u_j + \frac{2}{5}u_{j-1} = \frac{-u_{j+2} + 12u_{j+1} + 36u_j - 44u_{j-1} - 3u_{j-2}}{60}, \tag{9}$$

with

$$\begin{aligned} u_j &= \frac{-\frac{1}{60}e^{2i\alpha} + \frac{12}{60}e^{i\alpha} + \frac{36}{60} - \frac{44}{60}e^{-i\alpha} - \frac{3}{60}e^{-2i\alpha}}{\frac{36}{60} + \frac{24}{60}e^{-i\alpha}}\hat{u}(t)e^{ikx_j} \\ &= \frac{1}{117 + 108\cos\alpha}\left(24 - 6\cos^3\alpha - 18\sin^2\alpha - 18\sin\alpha\right. \\ &\quad \left. + i\left(6\sin^3\alpha + 45\sin\alpha\cos\alpha + 180\sin\alpha\right)\right)\hat{u}(t)e^{ikx_j} \end{aligned} \tag{10}$$

where

$$k_r = \frac{2\left(1 - 3\cos\alpha + 3\cos^2\alpha - \cos^3\alpha\right)}{3(13 + 12\cos\alpha)}, \quad k_i = \frac{\sin\alpha\left(2\sin^2\alpha + 15\cos\alpha + 60\right)}{3(13 + 12\cos\alpha)}. \tag{11}$$

For the explicit third-order upwind scheme [7],

$$k_r = \frac{1}{6}(3-4\cos\alpha+\cos 2\alpha), \quad k_i = \frac{1}{6}(8\sin\alpha-\sin 2\alpha), \tag{12}$$

and for the explicit fifth-order upwind scheme, we have,

$$k_r = \frac{10-15\cos\alpha+6\cos 2\alpha-\cos 3\alpha}{30}, \quad k_i = \frac{45\sin\alpha-9\sin 2\alpha+\sin 3\alpha}{30}. \tag{13}$$

Figure 1 shows variations of k_r and k_i with the reduced wave number α for the above four schemes. We can see the fifth-order schemes can approximate the exact damping ($k_r^E = 0$) to higher waver numbers than the third-order schemes, and the compact schemes can approximate the exact dispersion relation ($k_i^E = \alpha$) better than the non-compact schemes.

Table 1 gives the upper limit of the reduced wave number, which corresponds to a point in **Figure 1** where k_r or k_i begins to reach 2% errors relative to their exact solutions respectively. Larger upper limit implies fewer grid points are needed to resolve a given physical structure. For example, to approximate the exact wave speed within 2% error, the ratio of grid points needed by the 5th-order upwind compact scheme to those needed by the 5th-order upwind biased scheme is $1.25/1.71 = 0.73$ in one dimensional case. In three-dimensional case, this ratio becomes $(1.25/1.71)^3 = 0.39$, resulting in significant saving in computer resources.

2.2. Central Compact Schemes

In this section, various compact finite difference schemes are studied. The family of cell centered central compact schemes given by Lele *et al.* [3] is given by:

$$\nu u'_{i-2} + \mu u'_{i-1} + u'_i + \mu u'_{i+1} + \nu u'_{i+2} = c\frac{u_{i+3}-u_{i-3}}{6h} + c\frac{u_{i+2}-u_{i-2}}{4h} + c\frac{u_{i+1}-u_{i-1}}{2h} \tag{14}$$

The order of these schemes can be based parameters values as shown in **Table 2**.

Taking Fourier transform of Equation (14), we have

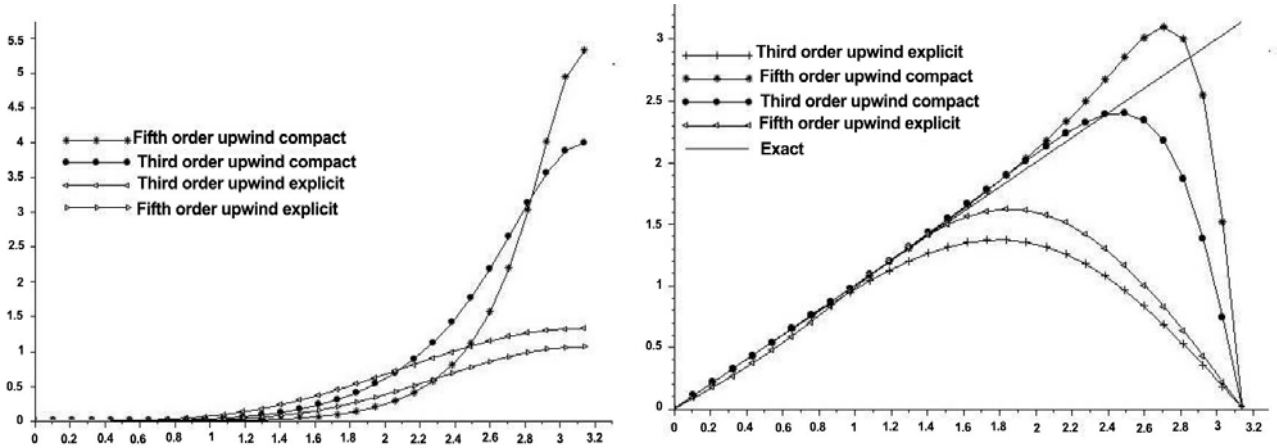

Figure 1. Variations of k_r and k_i vs. α for the compact and non-compact schemes.

Table 1. Upper limits of the reduced wave number when k_r and k_i of the difference schemes first exceed 2% errors relative to exact solutions.

Scheme	Upper limits of wave number	
	$k_r < 2\%$	$\lvert 1 - k_i/\alpha \rvert < 2\%$
5th-order upwind compact	1.35	1.71
3rd-order upwind compact	0.91	1.61
5th-order upwind	1.08	1.25
3rd-order upwind	0.72	0.902

Table 2. Values of parameters involved for the central compact scheme.

Order of scheme	μ	ν	a	b	c
2nd order	0	0	1	0	0
4th order	0	0	$\frac{4}{3}$	$\frac{1}{3}$	0
6th order	$\frac{1}{3}$	0	$\frac{14}{9}$	$\frac{1}{9}$	0
8th order	$\frac{4}{9}$	$\frac{1}{36}$	$\frac{40}{27}$	$\frac{25}{54}$	0
10th order	$\frac{1}{2}$	$\frac{1}{20}$	$\frac{17}{20}$	$\frac{191}{150}$	$\frac{1}{100}$

$$k_i = \frac{a\sin\alpha + \frac{b}{2}\sin 2\alpha + \frac{c}{3}\sin 3\alpha}{1 + 2\mu\cos\alpha + 2\nu\cos 2\alpha};\ k_r = 0. \tag{15}$$

The different values of k_i are given in Table 3.

The difference between modified wave number and exact wave number is very small, therefore these schemes have spectral like resolution. The comparison of various central compact schemes is presented in Figure 2. The eighth-order central compact scheme seems to follow the exact wave number more closely than all other central compact schemes, though it has a broader stencil width.

2.3. Comparison of Upwind and Central Compact Scheme

In this subsection, the upwind and central compact schemes are compared based upon the resolution characteristics k_i vs α. For this purpose, two upwind compact schemes and two central compact schemes are selected from the previous sections.

The comparison plot for k_i vs α is shown in Figure 3.

The comparison of the scheme enables us to find the scheme best suitable from the chosen schemes. Figure 3 shows that the upwind compact schemes give the better resolution amongst all the schemes while central compact schemes have poor resolution. So in order to improve the resolution of central schemes, filtering is required.

3. Conclusion

We have analyzed upwind, upwind compact and central compact schemes of

Table 3. Values of parameters involved for the central compact scheme.

Order of scheme	k_i
2nd order	$\sin\alpha$
4th order	$\frac{8\sin\alpha+\sin 2\alpha}{6}$
6th order	$\frac{\frac{14}{9}\sin\alpha+\frac{1}{18}\sin 2\alpha}{1+\frac{2}{3}\cos\alpha}$
8th order	$\frac{\frac{40}{27}\sin\alpha+\frac{25}{108}\sin 2\alpha}{1+\frac{8}{9}\cos\alpha+\frac{1}{18}\cos\alpha}$
10th order	$\frac{\frac{17}{12}\sin\alpha+\frac{191}{300}\sin 2\alpha+\frac{1}{300}\sin 3\alpha}{1+\cos\alpha+\frac{1}{10}\cos 2\alpha}$

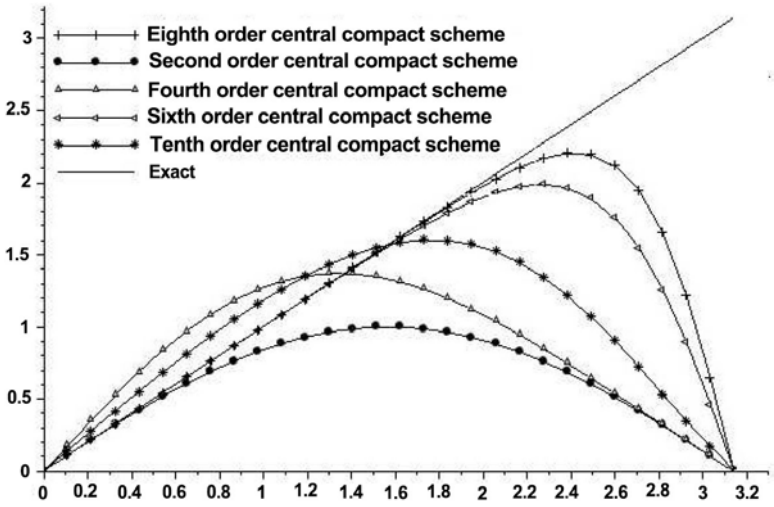

Figure 2. Comparison of various central compact schemes for k_i vs α.

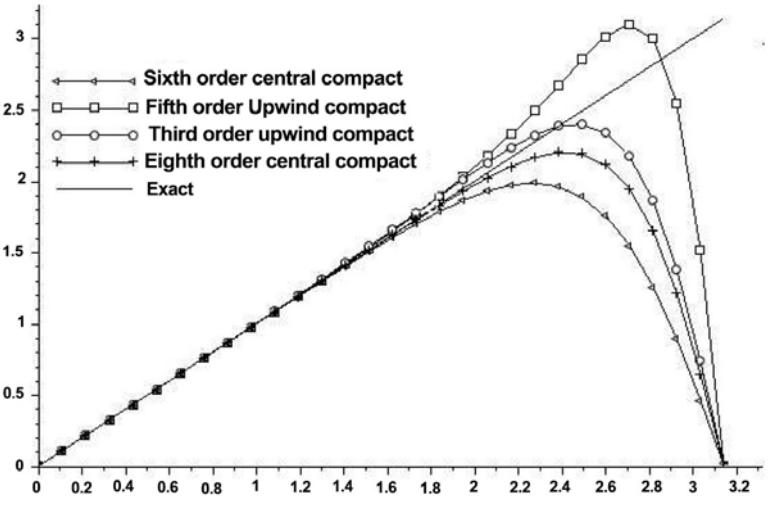

Figure 3. Comparison of upwind and central compact schemes k_i versus α.

different order accuracy for numerical investigation of convection equation. It is observed that the use of the upwind compact scheme makes the numerical solution more stable as compared with the central scheme and can be used for convection dominated problems. A comparison is also given with non-compact schemes of the same order of accuracy with almost the same computational cost.

Acknowledgments

The work of Abdullah Shah is supported by HEC under NRPU No. 7781 and PSF No. 5651.

Conflicts of Interest

The authors declare no conflicts of interest regarding the publication of this paper.

References

[1] Hirsh, R.S. (1975) High Order Accurate Difference Solutions of Fluid Mechanics Problems by a Compact Differencing Technique. *Journal of Computational Physics*, **19**, 90-109. https://doi.org/10.1016/0021-9991(75)90118-7

[2] Rubin, S.G. and Khosla, P.K. (1977) Polynomial Interpolation Methods for Viscous Flow Calculations. *Journal of Computational Physics*, **2**, 217-244. https://doi.org/10.1016/0021-9991(77)90036-5

[3] Lele, S.K. (1992) Compact Finite Difference Schemes with Spectral-Like Resolution. *Journal of Computational Physics*, **103**, 16-42. https://doi.org/10.1016/0021-9991(92)90324-R

[4] Sheng, T.Y. (1991) Runge-Kutta Methods Combined with Compact Difference Schemes for the Unsteady Euler Equations. *Center for Modeling of Turbulence and Transition-Research Briefs*, **93**, 15802.

[5] Zhou, Q., Yao, Z.F. and Shen, M.Y. (2007) A New Family of High-Order Compact Upwind Difference Schemes with Good Spectral Resolution. *Journal of Computational Physics*, **227**, 1306-13391. https://doi.org/10.1016/j.jcp.2007.09.008

[6] Shah, A., Yuan, L. and Islam, S. (2012) Numerical Solution of Unsteady Navier-Stokes Equations on Curvilinear Meshes. *Journal of Computer and Mathematics with applications*, **63**, 1548-1556. https://doi.org/10.1016/j.camwa.2012.03.047

[7] Fu, D.X. and Ma, Y.W. (1997) A High-Order Accurate Difference Scheme for Complex Flowfields. *Journal of Computational Physics*, **134**, 1-5. https://doi.org/10.1006/jcph.1996.5492

[8] Shah, A. and Yuan, L. (2010) Upwind Compact Finite Difference Scheme for Time-Dependent Incompressible Navier-Stokes Equations. *Applied Mathematics and Computation*, **215**, 3201-3213. https://doi.org/10.1016/j.amc.2009.10.001

[9] Rizwan, M., Shah, A. and Yuan, L. (2016) A Central Compact Scheme for Numerical Solution of Two-Phase Incompressible Flow Using Allen-Cahn Phase Field Model. *Journal of the Brazilian Society of Mechanical Sciences and Engineering*, **38**, 433-441. https://doi.org/10.1007/s40430-015-0342-4

[10] Khan, S. and Shah, A. (2019) Simulation of the Two-Dimensional Rayleigh-Taylor Instability Problem by Using Diffuse-Interface Model. *AIP Advances*, **9**, Article ID: 085312. https://doi.org/10.1063/1.5100791

[11] Saeed, S., Shah, A. and Khan, S. (2018) Numerical Investigation of Bubbles Coalescence in a Shear Flow with Diffuse-Interface Model. *Heliyon*, **4**, e01024. https://doi.org/10.1016/j.heliyon.2018.e01024

[12] Borujerdi, A.N. and Kebriaee, A. (2003) Upwind Compact Implicit and Explicit High Order Finite Difference Scheme for Level Set Techniques. *International Journal for Computational Methods in Engineering Science and Mechanics*, **3**, 308-318.

[13] De, A.K. and Eswaran, V. (2006) Analysis of a New High Resolution Upwind Compact Scheme. *Journal of Computational Physics*, **218**, 398-416. https://doi.org/10.1016/j.jcp.2006.02.020

[14] Gaitonde, D.V. and Visbal, M.R. (2000) Pade-Type Higher-Order Boundary Filters for the Navier Stokes Equations. *AIAA Journal*, **38**, 2103-2112.

[15] Liang, X., Zhang, S., Zhang, H. and Shu, C. (2013) A New Class of Central Compact Scheme with Spectral Like Resolution I. Linear Schemes. *Journal of Computational Physics*, **248**, 235-256. https://doi.org/10.1016/j.jcp.2013.04.014

[16] Shah, A. and Yuan, L. (2009) Flux-Difference Splitting Based Upwind Compact Scheme for the Incompressible Navier-Stokes Equations. *International Journal for Computational Methods in Engineering Science and Mechanics*, **61**, 552-568. https://doi.org/10.1002/fld.1965

World Journal of Mechanics, 2019, 9, 267-284
https://www.scirp.org/journal/wjm
ISSN Online: 2160-0503
ISSN Print: 2160-049X

Elastic Collisions in Minkowski Momentum Space with Lorentz Transformations

Akihiro Ogura

Laboratory of Physics, Nihon University, Matsudo, Japan
Email: ogura.akihiro@nihon-u.ac.jp

How to cite this paper: Ogura, A. (2019) Elastic Collisions in Minkowski Momentum Space with Lorentz Transformations. *World Journal of Mechanics*, **9**, 267-284.
https://doi.org/10.4236/wjm.2019.912018

Received: November 15, 2019
Accepted: December 16, 2019
Published: December 19, 2019

Abstract

We reexamined the elastic collision problems in the special relativity for both one and two dimensions from a different point of view. In order to obtain the final states in the laboratory system of the collision problems, almost all textbooks in the special relativity calculated the simultaneous equations. In contrast to this, we make a detour through the center-of-mass system. The two frames of references are connected by the Lorentz transformation with the velocity of the center-of-mass. This route for obtaining the final states is easy for students to understand the collision problems. For one dimensional case, we also give an example for illustrating the states of the particles in the Minkowski momentum space, which shows the whole story of the collision.

Keywords

Relativistic Elastic Collision, Minkowski Momentum Space, Lorentz Transformation

1. Introduction

Collisions of the interacting particles have fundamental importance in both classical mechanics and special relativity. Illustrating the collision problems is rewarding to understand them clearly and quickly.

For one dimensional collision in classical mechanics, mass-momentum diagram plays a key role [1] [2]. We can see the whole story of the collision in the single diagram for both the center-of-mass and the laboratory systems. For two dimensional collision in classical mechanics, two-dimensional momentum space describes the collision clearly in the textbook [3]. We also see the slightly different illustration which lays emphasis on the transformation of the two systems [4]. For one dimensional collision in the special relativity, Saletan [5] proposed to understand the collision problems in the Minkowski momentum space, with

energy E/c represented along the vertical axis and momentum p represented along the horizontal axis. The states of the particles are expressed by the arrow in the space. The quantitative application of it is stated by [6]. We do not need any calculation for obtaining the whole story of the collision. For two dimensional collision in the special relativity, illustration is clearly stated in the literature [6] [7]. We also see the slightly different illustration which lays emphasis on the transformation of the two systems [8].

In this article, we propose a different point of view for the elastic collision problems in the special relativity. We make a detour through the center-of-mass system for obtaining the final states in the laboratory system. It is applicable to both one and two dimensional collisions. This method shows the unified way to think about collision problems.

Now, consider two reference frames K and K'. We assume that the frame K' moves in the x-direction at speed V with respect to the frame K. And let us assume the origins O and O' of the two reference frames coincide at time $t=0$. An event that occurs at some point is observed from both frames and is characterized by a set of coordinates (ct, x, y, z) and (ct', x', y', z') where c is the speed of light. The Lorentz transformation gives the relation between two coordinates and it is described by

$$\begin{pmatrix} ct' \\ x' \\ y' \\ z' \end{pmatrix} = \begin{pmatrix} \gamma & -\beta\gamma & 0 & 0 \\ -\beta\gamma & \gamma & 0 & 0 \\ 0 & 0 & 1 & 0 \\ 0 & 0 & 0 & 1 \end{pmatrix} \begin{pmatrix} ct \\ x \\ y \\ z \end{pmatrix}, \tag{1}$$

where $\beta = V/c$ and $\gamma = 1/\sqrt{1-\beta^2}$. In the following paper, we designate the frame K as the laboratory system, while K' as the center-of-mass system. Accordingly, the velocity V describes the velocity of the center-of-mass. The inverse transformation is given by just putting $-\beta$ to β in Equation (1).

Our strategy is pictorially stated in **Figure 1**. In the textbooks of physics, we have to calculate the simultaneous equations of momentum- and energy-conservation in order to obtain the final states in the laboratory system. See the dashed arrow in **Figure 1**. Our strategy is as follows.

1) By the Lorentz inverse transformation, we obtain the velocity V of the center-of-mass in terms of energies (E_A, E_B) and momenta (p_A, p_B) in the laboratory system *before* the collision. The velocity V does not change throughout the collision.

2) By the Lorentz transformation, we obtain the momenta (p_A^*, p_B^*) in the center-of-mass system *before* the collision. See the strategy 2 in **Figure 1**. In this frame, two particles make a head on collision with the same magnitude of the momentum p^*.

3) We determine the momenta ($p_A'^*$, $p_B'^*$) in the center-of-mass system *after* the collision. See the strategy 3 in **Figure 1**. In this frame, two particles move the opposite direction with the same momentum p^* after the collision. We introduce the collision angle θ^* of the incident particle for the two dimensional case.

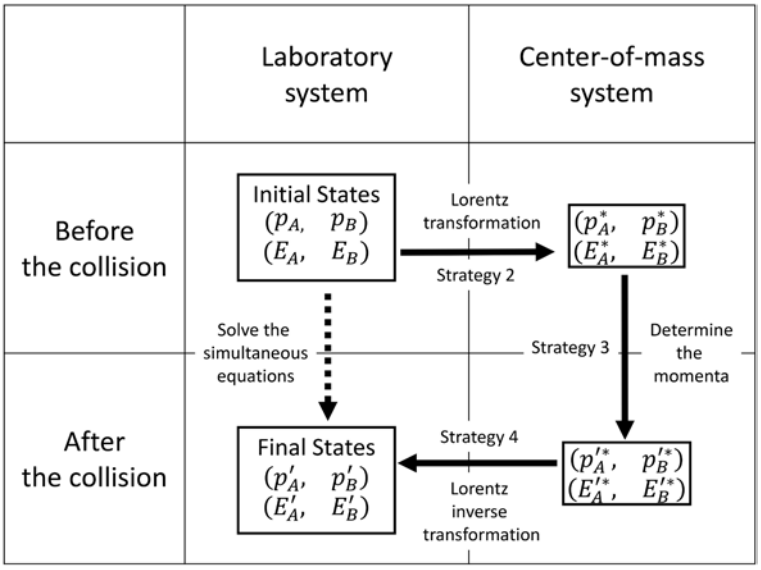

Figure 1. The usual approach to the collision problems is along the dashed arrow. The strategy in this article is on the detour of the solid arrows.

4) By the Lorentz inverse transformation, we obtain the momenta (p_A', p_B') in the laboratory system *after* the collision. See the strategy 4 in **Figure 1**. Finally, we reach the final states. We never solve the simultaneous equations in contrast with the usual treatment of the collision problems.

5) Let us consider the two special cases. One is that the target particle is at rest ($p_B = 0$) in the laboratory system before the collision. The other is that, in addition to the condition above, two particles have equal masses.

6) We check the limit $c \to \infty$ and see whether these strategies recover the Newtonian mechanics.

This paper is organized in the following way. In Section 2, we discuss one dimensional collisions, according to the strategy stated above. We also show the illustration of these collisions in Minkowski momentum space. This diagram shows the whole story of the one dimensional collision in the special relativity. In Section 3, we turn to the two dimensional collision case. We introduce the collision angle θ^* of the incident particle in the center-of-mass system. We show the theoretical background for the diagrammatic approach [6] [7] [8]. Section 4 is devoted to a summary.

2. Elastic Collisions in One Dimension

Let us discuss the one dimensional elastic collisions. The motions of the particles are restricted in the *x*-direction. Therefore, the *y*- and *z*-components of the momentum are zero. Although the illustrations of the contents of this section are already done by [5] [6], we reexamined how we draw the collision problems in the Minkowski momentum space.

2.1. Velocity of Center-of-Mass System

We discuss the strategy 1 in the Introduction. Consider the Lorentz inverse

transformation with the whole two body system,

$$\begin{pmatrix} \frac{E_A}{c}+\frac{E_B}{c} \\ p_A+p_B \\ 0 \\ 0 \end{pmatrix} = \begin{pmatrix} \gamma & \beta\gamma & 0 & 0 \\ \beta\gamma & \gamma & 0 & 0 \\ 0 & 0 & 1 & 0 \\ 0 & 0 & 0 & 1 \end{pmatrix} \begin{pmatrix} \frac{E_A^*}{c}+\frac{E_B^*}{c} \\ p_A^*+p_B^* \\ 0 \\ 0 \end{pmatrix}. \tag{2}$$

Here, $p_A^*+p_B^*=0$ is the definition of the center-of-mass system. From the matrix, we obtain the following relations:

$$p_A+p_B=\beta\gamma\left(\frac{E_A^*}{c}+\frac{E_B^*}{c}\right), \tag{3}$$

$$\frac{E_A}{c}+\frac{E_B}{c}=\gamma\left(\frac{E_A^*}{c}+\frac{E_B^*}{c}\right). \tag{4}$$

Dividing these equations, we obtain the velocity of the center-of-mass

$$\beta=\frac{V}{c}=\frac{p_A+p_B}{\frac{E_A}{c}+\frac{E_B}{c}}, \tag{5}$$

which is conserved throughout the collision because of the conservation law of energy and momentum. Moreover, we define the following conserved quantity:

$$s\equiv\left(\frac{E_A^*}{c}+\frac{E_B^*}{c}\right)^2=\left(\frac{E_A}{c}+\frac{E_B}{c}\right)^2-\left(p_A+p_B\right)^2, \tag{6}$$

$$=m_A^2c^2+m_B^2c^2+2\left(\frac{E_A}{c}\frac{E_B}{c}-p_Ap_B\right), \tag{7}$$

where m_A and m_B are the masses of the colliding particles. We used the relation $\left(E/c\right)^2-p^2=\left(mc\right)^2$, which is satisfied by the relativistic particle. When we define W as the total energy in the center-of-mass system, then W is written in terms of s as follows:

$$W\equiv E_A^*+E_B^*=c\sqrt{s}. \tag{8}$$

We also calculate the following quantities from Equation (5),

$$\gamma=\frac{1}{\sqrt{1-\beta^2}}=\frac{\frac{E_A}{c}+\frac{E_B}{c}}{\sqrt{s}},\quad \beta\gamma=\frac{p_A+p_B}{\sqrt{s}}, \tag{9}$$

which are frequently used in the following sections.

Figure 2 depicts the states of two particles before the collision in the laboratory system:

$$\boldsymbol{OA}=\left(\frac{E_A}{c},p_A,0,0\right),\quad \boldsymbol{OB}=\left(\frac{E_B}{c},p_B,0,0\right). \tag{10}$$

According to the parallelogram law, we obtain the vector $\boldsymbol{OC}=\boldsymbol{OA}+\boldsymbol{OB}$, which indicates the state of the center-of-mass. The β in Equation (5) is understood by $\beta=\tan\theta$ in Figure 2. Moreover, the vector $\boldsymbol{OC}$ shows the case

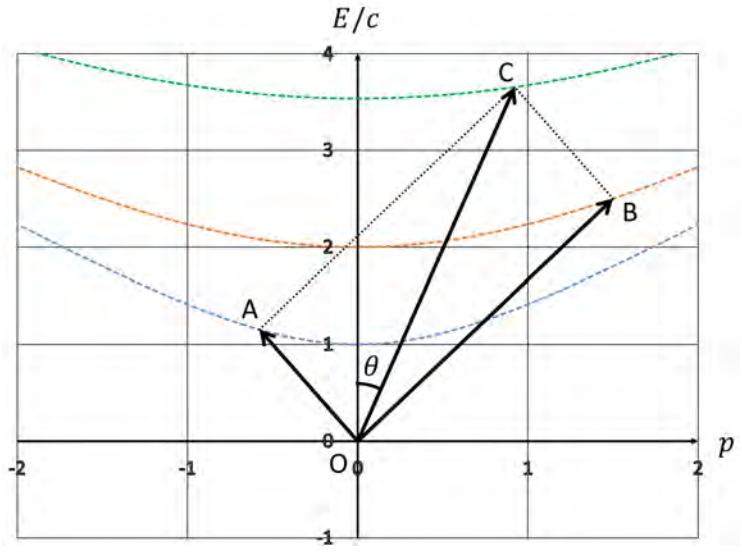

Figure 2. Figure shows the case in [6]: $m_A = 1$, $v_A = -0.5c$, $m_B = 2$, $v_B = 0.6c$. The tips A and B show the states of the particles before the collision in the laboratory system. The tip C is determined from A and B by the parallelogram law.

of the perfect inelastic collision in the special relativity, *i.e.*, the two particles are combined and move with the velocity β after the collision. Contrary to this, this diagram is also interpreted as the decay process. The parent particle $\boldsymbol{OC}$ decays into two daughter particles $\boldsymbol{OA}$ and $\boldsymbol{OB}$.

2.2. Momenta and Energies in the Center-of-Mass System before the Collision

We discuss the strategy 2 in the Introduction. Concerning the Lorentz transformation for each particle,

$$\begin{pmatrix} \frac{E_A^*}{c} \\ p_A^* \\ 0 \\ 0 \end{pmatrix} = \begin{pmatrix} \gamma & -\beta\gamma & 0 & 0 \\ -\beta\gamma & \gamma & 0 & 0 \\ 0 & 0 & 1 & 0 \\ 0 & 0 & 0 & 1 \end{pmatrix} \begin{pmatrix} \frac{E_A}{c} \\ p_A \\ 0 \\ 0 \end{pmatrix}, \quad \begin{pmatrix} \frac{E_B^*}{c} \\ p_B^* \\ 0 \\ 0 \end{pmatrix} = \begin{pmatrix} \gamma & -\beta\gamma & 0 & 0 \\ -\beta\gamma & \gamma & 0 & 0 \\ 0 & 0 & 1 & 0 \\ 0 & 0 & 0 & 1 \end{pmatrix} \begin{pmatrix} \frac{E_B}{c} \\ p_B \\ 0 \\ 0 \end{pmatrix}, \tag{11}$$

we obtain the momenta in the center-of-mass system before the collision;

$$p_A^* = -\beta\gamma \frac{E_A}{c} + \gamma p_A = + \frac{p_A \frac{E_B}{c} - p_B \frac{E_A}{c}}{\sqrt{s}}, \tag{12}$$

$$p_B^* = -\beta\gamma \frac{E_B}{c} + \gamma p_B = - \frac{p_A \frac{E_B}{c} - p_B \frac{E_A}{c}}{\sqrt{s}}, \tag{13}$$

where we used Equations (9). It is natural that $p_A^* + p_B^* = 0$ is fulfilled because of the definition of the center-of-mass system. Then we define a momentum p^* as

$$p^* \equiv \frac{p_A \frac{E_B}{c} - p_B \frac{E_A}{c}}{\sqrt{s}} = p_A^* = -p_B^*, \tag{14}$$

for later use. The energies of the particles in the system are also given by Equations (11),

$$\frac{E_A^*}{c} = \gamma \frac{E_A}{c} - \beta\gamma p_A = \frac{\frac{E_A}{c}\frac{E_B}{c} - p_A p_B + m_A^2 c^2}{\sqrt{s}} = \frac{s + m_A^2 c^2 - m_B^2 c^2}{2\sqrt{s}}, \tag{15}$$

$$\frac{E_B^*}{c} = \gamma \frac{E_B}{c} - \beta\gamma p_B = \frac{\frac{E_A}{c}\frac{E_B}{c} - p_A p_B + m_B^2 c^2}{\sqrt{s}} = \frac{s - m_A^2 c^2 + m_B^2 c^2}{2\sqrt{s}}, \tag{16}$$

where we used Equations (7) and (9). These energies are also derived by $E_A^*/c = \sqrt{\left(p^*\right)^2 + m_A^2 c^2}$ and $E_B^*/c = \sqrt{\left(p^*\right)^2 + m_B^2 c^2}$ with Equations (12) and (13). Summing up these energies, we can easily see Equation (8).

We obtain these results from Figure 3. We draw a new p^*-axis which has the slope $\tan\theta$ with respect to the horizontal p-axis. Drawing the dotted line from the tips A and B to the p^*-axis in parallel to the line OC, the crossing points indicate the momenta p_A^* and p_B^* whose distances from the origin O are equal. This means $p_A^* + p_B^* = 0$. Moreover, we draw the dotted line from the tips A and B to the line OC in parallel to the p^*-axis. The crossing points A'' and B'' describe the energies E_A^*/c and E_B^*/c in the center-of-mass system before the collision.

2.3. Momenta and Energies in the Center-of-Mass System after the Collision

We discuss the strategy 3 in the Introduction. We determine the momenta in the

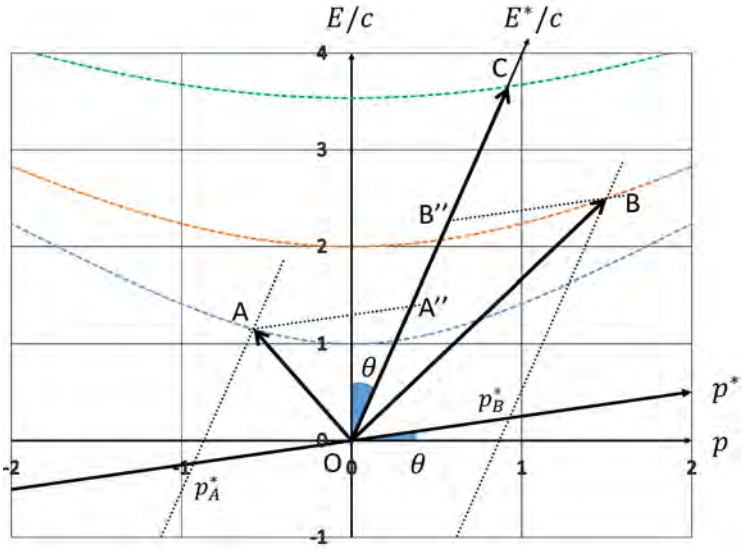

Figure 3. Draw the line from the tips of the vectors A and B to the p^*-axis in parallel to the line OC. The crossing points with p^*-axis show the momenta of each particle in the center-of-mass system.

center-of-mass system after the collision. In this frame, the particles move in the opposite direction after the collision with the same magnitude of p^* in Equation (14). We write down the momenta in the center-of-mass system after the collision

$$p_A'^* \equiv -p_A^* = -p^*, \quad p_B'^* \equiv -p_B^* = +p^*. \tag{17}$$

Since the magnitudes of the momenta do not change, the energies of the particles

$$E_A'^* = E_A^*, \quad E_B'^* = E_B^* \tag{18}$$

do not change either in this frame, where E_A^* and E_B^* are given by equations (15) and (16).

2.4. Momenta and Energies in the Laboratory System after the Collision

We discuss the strategy 4 in the Introduction. Consider the Lorentz inverse transformation for each particle,

$$\begin{pmatrix} \frac{E_A'}{c} \\ p_A' \\ 0 \\ 0 \end{pmatrix} = \begin{pmatrix} \gamma & \beta\gamma & 0 & 0 \\ \beta\gamma & \gamma & 0 & 0 \\ 0 & 0 & 1 & 0 \\ 0 & 0 & 0 & 1 \end{pmatrix} \begin{pmatrix} \frac{E_A'^*}{c} \\ p_A'^* \\ 0 \\ 0 \end{pmatrix}, \quad \begin{pmatrix} \frac{E_B'}{c} \\ p_B' \\ 0 \\ 0 \end{pmatrix} = \begin{pmatrix} \gamma & \beta\gamma & 0 & 0 \\ \beta\gamma & \gamma & 0 & 0 \\ 0 & 0 & 1 & 0 \\ 0 & 0 & 0 & 1 \end{pmatrix} \begin{pmatrix} \frac{E_B'^*}{c} \\ p_B'^* \\ 0 \\ 0 \end{pmatrix}, \tag{19}$$

we obtain the momenta in the laboratory system after the collision. From the second row of these matrices, we obtain

$$\begin{aligned} p_A' &= \beta\gamma \frac{E_A'^*}{c} + \gamma p_A'^* \\ &= \frac{p_A + p_B}{\sqrt{s}} \times \frac{\frac{E_A}{c}\frac{E_B}{c} - p_A p_B + m_A^2 c^2}{\sqrt{s}} - \frac{\frac{E_A}{c} + \frac{E_B}{c}}{\sqrt{s}} \times \frac{p_A \frac{E_B}{c} - p_B \frac{E_A}{c}}{\sqrt{s}}, \end{aligned} \tag{20}$$

$$\begin{aligned} p_B' &= \beta\gamma \frac{E_B'^*}{c} + \gamma p_B'^* \\ &= \frac{p_A + p_B}{\sqrt{s}} \times \frac{\frac{E_A}{c}\frac{E_B}{c} - p_A p_B + m_B^2 c^2}{\sqrt{s}} + \frac{\frac{E_A}{c} + \frac{E_B}{c}}{\sqrt{s}} \times \frac{p_A \frac{E_B}{c} - p_B \frac{E_A}{c}}{\sqrt{s}}, \end{aligned} \tag{21}$$

where we used Equations (9), (17) and (18). Adding the two equations, we easily see the conservation of momentum: $p_A' + p_B' = p_A + p_B$. Moreover, we also obtain the energies from Equations (19),

$$\begin{aligned} \frac{E_A'}{c} &= \gamma \frac{E_A'^*}{c} + \beta\gamma p_A'^* \\ &= \frac{\frac{E_A}{c} + \frac{E_B}{c}}{\sqrt{s}} \times \frac{\frac{E_A}{c}\frac{E_B}{c} - p_A p_B + m_A^2 c^2}{\sqrt{s}} - \frac{p_A + p_B}{\sqrt{s}} \times \frac{p_A \frac{E_B}{c} - p_B \frac{E_A}{c}}{\sqrt{s}}, \end{aligned} \tag{22}$$

$$\frac{E'_B}{c} = \gamma \frac{E'^*_B}{c} + \beta\gamma p'^*_B$$
$$= \frac{\frac{E_A}{c} + \frac{E_B}{c}}{\sqrt{s}} \times \frac{\frac{E_A}{c}\frac{E_B}{c} - p_A p_B + m_B^2 c^2}{\sqrt{s}} + \frac{p_A + p_B}{\sqrt{s}} \times \frac{p_A \frac{E_B}{c} - p_B \frac{E_A}{c}}{\sqrt{s}}, \quad (23)$$

where we used Equations (9), (17) and (18). We easily check the conservation of energy: $\frac{E'_A}{c} + \frac{E'_B}{c} = \frac{E_A}{c} + \frac{E_B}{c}$.

Figure 4 shows the whole story of the one dimensional collision. Since the momenta of the particles exchange in the center-of-mass system after the collision, the tips A and B', B and A' are on the same dotted line. Thus, the dashed vectors

$$\boldsymbol{OA'} = \left(\frac{E'_A}{c}, p'_A, 0, 0\right), \quad \boldsymbol{OB'} = \left(\frac{E'_B}{c}, p'_B, 0, 0\right) \quad (24)$$

show the states after the collision. Namely, the tip $A(B)$ can slide on the hyperbola $\left(E_{A(B)}/c\right)^2 - p^2_{A(B)} = m^2_{A(B)}c^2$ until the tip $\boldsymbol{A'(B')}$. Furthermore, the sum of these vectors $\boldsymbol{OA'} + \boldsymbol{OB'}$ equals $\boldsymbol{OC}$, which means that $\boldsymbol{OC}$ is not altered throughout the collision.

The point $\boldsymbol{A''(B'')}$ is the midpoint of the line $\boldsymbol{AA'(BB')}$ which means that the energies in the center-of-mass system do not change before and after the collision, *i.e.*, Equation (18).

Once the momenta and energies of the particles before the collision are given, we obtain the final states as shown in Figure 4 without any calculations.

2.5. In Case of $p_B = 0$

We discuss the strategy 5 in the Introduction. In this case, we substitute $E_B = m_B c^2$ into the equations of this section. Equation (7) becomes simple form

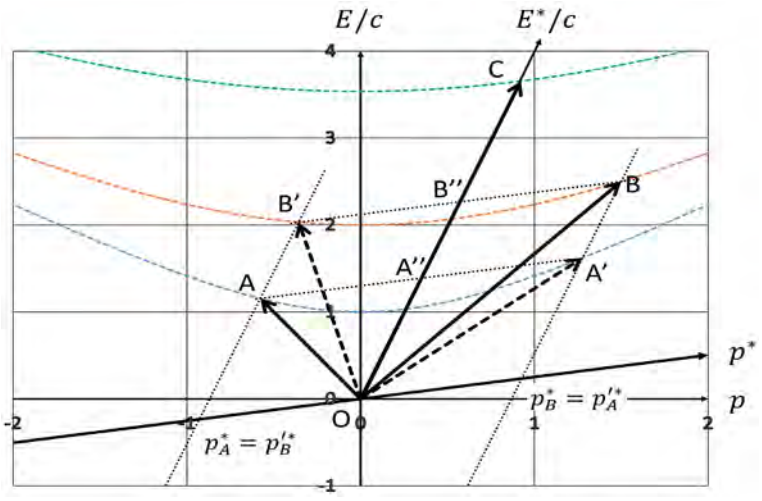

Figure 4. The solid and dashed arrows show the states of the particles before and after the collision.

$$s = m_A^2 c^2 + m_B^2 c^2 + 2m_B c \frac{E_A}{c}, \tag{25}$$

and we obtain the relation

$$\beta\gamma \frac{E_B^*}{c} = \gamma p^* = \frac{\left(\frac{E_A}{c} + m_B c\right) p_A m_B c}{s}. \tag{26}$$

From Equations (20) and (21), we obtain the momenta in the laboratory system after the collision

$$p_A' = \frac{m_A^2 c^2 - m_B^2 c^2}{s} \times p_A = p_A - \frac{2m_B c\left(\frac{E_A}{c} + m_B c\right)}{s} \times p_A, \tag{27}$$

$$p_B' = \frac{2m_B c\left(\frac{E_A}{c} + m_B c\right)}{s} \times p_A. \tag{28}$$

The second term of the right hand side of Equation (27) is a momentum lost by the particle A, and this transfers to the momentum gained by the particle B in Equation (28). This is the impulse in the special relativity. We obviously understand the conservation of the momentum: $p_A' + p_B' = p_A$. In addition, we obtain the energies from Equations (22) and (23)

$$\frac{E_A'}{c} = \frac{E_A}{c} - \frac{2m_B c}{s} \times p_A^2, \tag{29}$$

$$\frac{E_B'}{c} = m_B c + \frac{2m_B c}{s} \times p_A^2. \tag{30}$$

The second terms of the right hand side of both equations are the same and it transfers from the particle A to B. This is the work in the special relativity. The sum of these energies $\frac{E_A'}{c} + \frac{E_B'}{c} = \frac{E_A}{c} + m_B c$ shows the conservation law of energy.

Figure 5 shows the Minkowski momentum diagram in this case. The vector ***OB*** is along the vertical axis, which means $p_B = 0$ before the collision.

2.6. In Case of $p_B = 0$ and $m_A = m_B = m$

The quantity s becomes more simple form

$$s = 2mc\left(\frac{E_A}{c} + mc\right), \tag{31}$$

and we obtain the following relations

$$\beta\gamma \frac{E_A^*}{c} = \beta\gamma \frac{E_B^*}{c} = \gamma p^* = \frac{p_A}{2}. \tag{32}$$

We obtain the momenta

$$p_A' = 0, \quad p_B' = p_A, \tag{33}$$

and energies

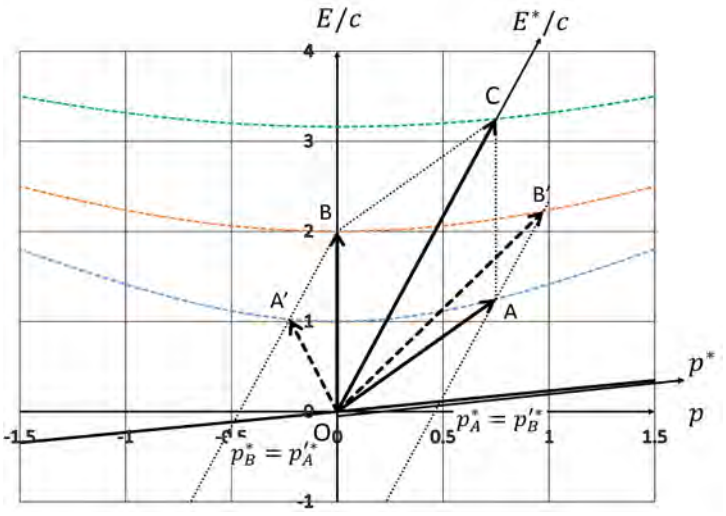

Figure 5. The solid and dashed arrows show the states of the particles before and after the collision in case of $p_B = 0$.

$$\frac{E_A'}{c} = mc, \quad \frac{E_B'}{c} = \frac{E_A}{c}, \tag{34}$$

in the laboratory system. After the collision, the incident particle A stops and the initially rest particle B moves with the momentum of which the particle A had before the collision.

2.7. In the Limit $c \to \infty$

In the limit $c \to \infty$, the relativistic energy E is replaced by mc^2. Equation (5) becomes

$$V = \frac{p_A c + p_B c}{\frac{E_A}{c} + \frac{E_B}{c}} \to \frac{p_A c + p_B c}{m_A c + m_B c} = \frac{p_A + p_B}{m_A + m_B}. \tag{35}$$

This is the velocity of the center-of-mass in Newtonian mechanics. Equation (7) shows

$$s \to m_A^2 c^2 + m_B^2 c^2 + 2 m_A c m_B c - 2 p_A p_B = \left(m_A + m_B\right)^2 c^2 - 2 p_A p_B, \tag{36}$$

then, the Lorentz factors Equations (9) become

$$\gamma \to \frac{m_A c + m_B c}{\sqrt{\left(m_A + m_B\right)^2 c^2 - 2 p_A p_B}} = \frac{m_A + m_B}{\sqrt{\left(m_A + m_B\right)^2 - 2 p_A p_B / c^2}} \to 1,$$

$$\beta\gamma \to \frac{p_A + p_B}{\sqrt{\left(m_A + m_B\right)^2 c^2 - 2 p_A p_B}} \to 0.$$

Equation (14) becomes

$$p^* \to \frac{p_A m_B c - p_B m_A c}{\sqrt{\left(m_A + m_B\right)^2 c^2 - 2 p_A p_B}} = \frac{p_A m_B - p_B m_A}{\sqrt{\left(m_A + m_B\right)^2 - 2 p_A p_B / c^2}} \to \frac{m_B p_A - m_A p_B}{m_A + m_B}, \tag{37}$$

which is the momentum in the center-of-mass system in Newtonian mechanics. Using these equations, we obtain the momenta Equations (20) and (21),

$$p'_A \to m_A \frac{p_A + p_B}{m_A + m_B} - \frac{m_B p_A - m_A p_B}{m_A + m_B} = m_A V - p^*, \tag{38}$$

$$p'_B \to m_B \frac{p_A + p_B}{m_A + m_B} + \frac{m_B p_A - m_A p_B}{m_A + m_B} = m_B V + p^*, \tag{39}$$

after the collision in the laboratory system, which are recovered the case in Newtonian mechanics.

3. Elastic Collisions in Two Dimensions

Let us turn our discussion to the case of the two dimensional elastic collisions. We suppose that the motions of the particles are restricted in the *x*-*y* plain, so that the *z*-component of the momentum is zero. Since the motions of the particles are supposed along the *x*-direction before the collision, we repeat the same discussion of Subsections 2.1 and 2.2. The illustration of this section is already done by [7] [8].

3.1. Momenta and Energies in the Center-of-Mass System after the Collision

Let us start our discussion from the strategy 3 in the Introduction. In the center-of-mass system, the magnitudes of the momenta do not change before and after the collision. Thus, we write down the momenta in the same way with Equation (14),

$$p^* \equiv \frac{p_A \dfrac{E_B}{c} - p_B \dfrac{E_A}{c}}{\sqrt{s}} = \left|p_A^*\right| = \left|p_B^*\right| = \left|p_A'^*\right| = \left|p_B'^*\right|, \tag{40}$$

where s is defined by Equation (7).

However, the direction of the momenta changes after the collision in two dimensions. As shown in **Figure 6**, we define the sense of the momentum $\boldsymbol{p}_A'^*$ as $\boldsymbol{n}^* = \left(\cos\theta^*, \sin\theta^*, 0\right)$, where θ^* is the scattering angle of the particle A in the center-of-mass system. In other words, the momenta after the collisions are denoted by the vector-form:

$$\boldsymbol{p}_A'^* = p^* \boldsymbol{n}^* = -\boldsymbol{p}_B'^*. \tag{41}$$

Since the magnitudes of the momenta do not change in this frame throughout the collision, the energies of each particle do not change either:

$$E_A'^* = E_A^*, \quad E_B'^* = E_B^*, \tag{42}$$

where E_A^* and E_B^* are given by Equations (15) and (16).

3.2. Momenta and Energies in the Laboratory System after the Collision

We discuss the strategy 4 in the Introduction. The motion of the particles after the collision is supposed to occur in the *x*-*y* plain. Thus, the momenta are

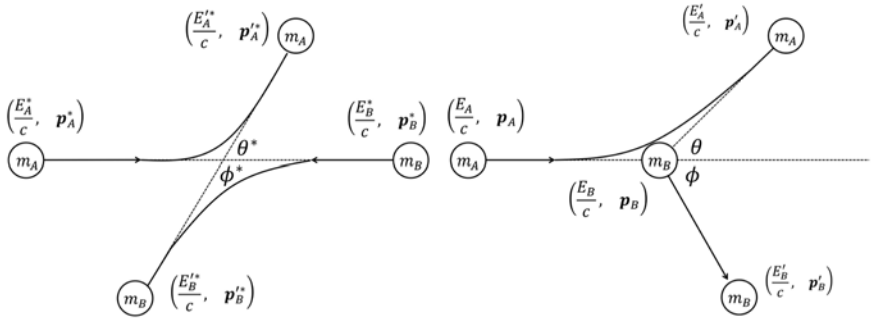

Figure 6. Left: The collision in the center-of-mass system. The scattering angles θ^* and ϕ^* have the relation $\theta^* + \phi^* = \pi$. Right: The collision in the laboratory system.

written by $\boldsymbol{p}'_A = \left(p'_{Ax}, p'_{Ay}, 0\right) = \left(p'_A \cos\theta, p'_A \sin\theta, 0\right)$ and $\boldsymbol{p}'_B = \left(p'_{Bx}, p'_{By}, 0\right) = \left(p'_B \cos\phi, -p'_B \sin\phi, 0\right)$, where θ and ϕ are the scattering angle of the particles A and B in the laboratory system as shown in Figure 6.

From the Lorentz inverse transformation, we obtain the momenta in the laboratory system after the collision by using Equation (41)

$$\begin{pmatrix} \frac{E'_A}{c} \\ p'_{Ax} \\ p'_{Ay} \\ 0 \end{pmatrix} = \begin{pmatrix} \frac{E'_A}{c} \\ p'_A \cos\theta \\ p'_A \sin\theta \\ 0 \end{pmatrix} = \begin{pmatrix} \gamma & \beta\gamma & 0 & 0 \\ \beta\gamma & \gamma & 0 & 0 \\ 0 & 0 & 1 & 0 \\ 0 & 0 & 0 & 1 \end{pmatrix} \begin{pmatrix} \frac{E^*_A}{c} \\ p^* \cos\theta^* \\ p^* \sin\theta^* \\ 0 \end{pmatrix}, \tag{43}$$

$$\begin{pmatrix} \frac{E'_B}{c} \\ p'_{Bx} \\ p'_{By} \\ 0 \end{pmatrix} = \begin{pmatrix} \frac{E'_B}{c} \\ p'_B \cos\phi \\ -p'_B \sin\phi \\ 0 \end{pmatrix} = \begin{pmatrix} \gamma & \beta\gamma & 0 & 0 \\ \beta\gamma & \gamma & 0 & 0 \\ 0 & 0 & 1 & 0 \\ 0 & 0 & 0 & 1 \end{pmatrix} \begin{pmatrix} \frac{E^*_B}{c} \\ -p^* \cos\theta^* \\ -p^* \sin\theta^* \\ 0 \end{pmatrix}. \tag{44}$$

From the second and third row of these matrices, we obtain x- and y-components of the momentum for the particle A,

$$p'_{Ax} = p'_A \cos\theta = \beta\gamma \frac{E^*_A}{c} + \gamma p^* \cos\theta^*, \tag{45}$$

$$p'_{Ay} = p'_A \sin\theta = p^* \sin\theta^*, \tag{46}$$

and for the particle B,

$$p'_{Bx} = p'_B \cos\phi = \beta\gamma \frac{E^*_B}{c} - \gamma p^* \cos\theta^*, \tag{47}$$

$$p'_{By} = -p'_B \sin\phi = -p^* \sin\theta^*. \tag{48}$$

Combining with the relation $\cos^2\theta^* + \sin^2\theta^* = 1$, we obtain

$$\left(\frac{p'_{Ax} - \beta\gamma \frac{E^*_A}{c}}{\gamma p^*}\right)^2 + \left(\frac{p'_{Ay}}{p^*}\right)^2 = 1, \tag{49}$$

$$\left(\frac{p'_{Bx}-\beta\gamma\frac{E^*_B}{c}}{\gamma p^*}\right)^2+\left(\frac{p'_{By}}{p^*}\right)^2=1. \tag{50}$$

These equations show the ellipse with the following parameters:

$$\text{minor semiaxis}\quad p^*=\frac{p_A\frac{E_B}{c}-p_B\frac{E_A}{c}}{\sqrt{s}}, \tag{51}$$

$$\text{major semiaxis}\quad \gamma p^*=\frac{\left(\frac{E_A}{c}+\frac{E_B}{c}\right)\left(p_A\frac{E_B}{c}-p_B\frac{E_A}{c}\right)}{s}, \tag{52}$$

$$\text{eccentricity}\quad \beta\gamma p^*=\frac{\left(p_A+p_B\right)\left(p_A\frac{E_B}{c}-p_B\frac{E_A}{c}\right)}{s}, \tag{53}$$

$$\text{midpoint of foci}\quad \beta\gamma\frac{E^*_A}{c}=\frac{\left(p_A+p_B\right)\left(\frac{E_A}{c}\frac{E_B}{c}-p_Ap_B+m_A^2c^2\right)}{s}, \tag{54}$$

$$\text{midpoint of foci}\quad \beta\gamma\frac{E^*_B}{c}=\frac{\left(p_A+p_B\right)\left(\frac{E_A}{c}\frac{E_B}{c}-p_Ap_B+m_B^2c^2\right)}{s}, \tag{55}$$

where Equations (7), (9), (14), (15) and (16) are used.

From the Lorentz transformation Equation (43) with Equation (15), we obtain the energy in the laboratory system after the collision

$$\begin{aligned}\frac{E'_A}{c}&=\gamma\frac{E^*_A}{c}+\beta\gamma p^*\cos\theta^*\\&=\gamma\left(\gamma\frac{E_A}{c}-\beta\gamma p_A\right)+\beta\gamma p^*\cos\theta^*\\&=\frac{E_A}{c}-\beta\gamma p^*\left(1-\cos\theta^*\right),\end{aligned} \tag{56}$$

where we used Equations (9). In the same manner, from Equations (44) and (16), we obtain

$$\begin{aligned}\frac{E'_B}{c}&=\gamma\frac{E^*_B}{c}-\beta\gamma p^*\cos\theta^*\\&=\gamma\left(\gamma\frac{E_B}{c}-\beta\gamma p_B\right)-\beta\gamma p^*\cos\theta^*\\&=\frac{E_B}{c}+\beta\gamma p^*\left(1-\cos\theta^*\right).\end{aligned} \tag{57}$$

The second terms of the right hand side in Equations (56) and (57) show the energy lost by the particle A and the energy gained by the particle B. This is the work in the special relativity. From these energies, we clearly see the conservation law of the energy: $\frac{E'_A}{c}+\frac{E'_B}{c}=\frac{E_A}{c}+\frac{E_B}{c}$.

3.3. In Case of $p_B = 0$

We discuss the strategy 5 in the Introduction. The parameters of the ellipse become simple form:

$$\text{minor semiaxis} \quad p^* = \frac{p_A m_B c}{\sqrt{s}}, \tag{58}$$

$$\text{major semiaxis} \quad \gamma p^* = \frac{\left(\frac{E_A}{c} + m_B c\right) p_A m_B c}{s} = \beta\gamma \frac{E_B^*}{c}, \tag{59}$$

$$\text{eccentricity} \quad \beta\gamma p^* = \frac{p_A^2 m_B c}{s}, \tag{60}$$

$$\text{midpoint of foci} \quad \beta\gamma \frac{E_A^*}{c} = \frac{p_A\left(\frac{E_A}{c} m_B c + m_A^2 c^2\right)}{s}, \tag{61}$$

where s is given by Equation (25). Equation (59) is as the same relation with Equation (26). The ellipse Equation (49) with these parameters is depicted in **Figure 7**. This is already done by [8].

3.4. In Case of $p_B = 0$ and $m_A = m_B = m$

The parameters of the ellipse are the followings:

$$\text{minor semiaxis} \quad p^* = \frac{p_A mc}{\sqrt{s}}, \tag{62}$$

$$\text{major semiaxis} \quad \gamma p^* = \frac{p_A}{2} = \beta\gamma \frac{E_B^*}{c}, \tag{63}$$

$$\text{eccentricity} \quad \beta\gamma p^* = \frac{\frac{E_A}{c} - mc}{2}, \tag{64}$$

$$\text{midpoint of foci} \quad \beta\gamma \frac{E_A^*}{c} = \frac{p_A}{2}, \tag{65}$$

where s is given by Equation (31). Equations (63) and (65) are as same as Equation (32).

Dividing Equations (45), (46) and Equations (47), (48), we obtain the relations of the scattering angles

$$\tan\theta = \frac{p^* \sin\theta^*}{\beta\gamma \frac{E_A^*}{c} + \gamma p^* \cos\theta^*} = \frac{\sin\theta^*/\gamma}{1 + \cos\theta^*}, \tag{66}$$

$$\tan\phi = \frac{p^* \sin\theta^*}{\beta\gamma \frac{E_B^*}{c} - \gamma p^* \cos\theta^*} = \frac{\sin\theta^*/\gamma}{1 - \cos\theta^*}. \tag{67}$$

Thus the product of these two equations becomes

$$\tan\theta \times \tan\phi = \frac{\sin^2\theta^*/\gamma^2}{1 - \cos^2\theta^*} = \frac{1}{\gamma^2} < 1. \tag{68}$$

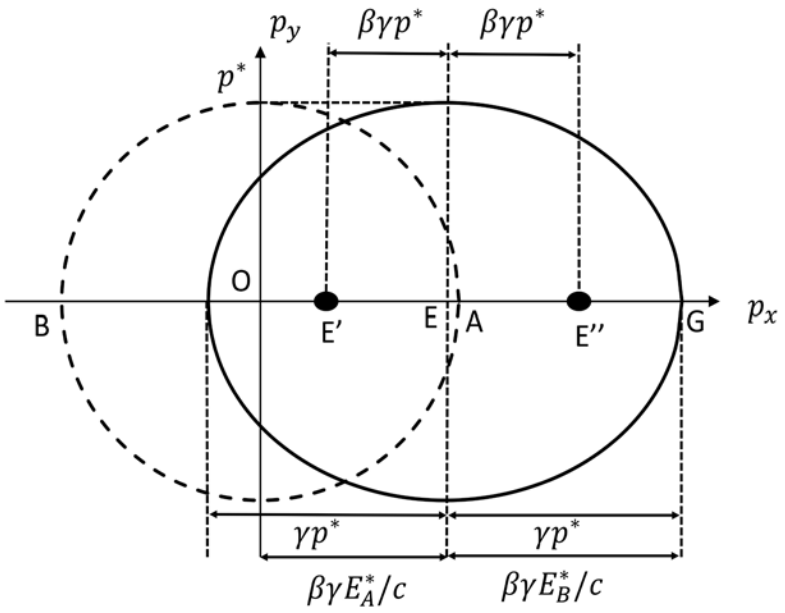

Figure 7. The ellipse Equation (49) with $p_B = 0$ is illustrated in the solid line. The points E' and E'' are the foci of this ellipse and the midpoint of them is depicted by E. The dashed circle shows the collision in the center-of-mass system [8].

Because of the relation of the tangent

$$\tan(\theta+\phi) = \frac{\tan\theta + \tan\phi}{1 - \tan\theta\tan\phi},$$

we obtain $\theta + \phi < \frac{\pi}{2}$, in contrast to the Newtonian case in which $\theta + \phi = \frac{\pi}{2}$.

3.5. In Case of $p_B = 0$ and $m_A = 0$: Compton Scattering

From the Lorentz inverse transformation in Equation (43), we obtain

$$\frac{E'_A}{c} = \gamma\frac{E_A^*}{c} + \beta\gamma p^*\cos\theta^*, \tag{69}$$

$$p'_A\cos\theta = \beta\gamma\frac{E_A^*}{c} + \gamma p^*\cos\theta^*. \tag{70}$$

Eliminating p^* and using Equation (15), we obtain

$$\begin{aligned}\frac{E'_A}{c} - \beta p'_A\cos\theta &= \gamma\left(1-\beta^2\right)\frac{E_A^*}{c}\\ &= \gamma\left(1-\beta^2\right)\left(\gamma\frac{E_A}{c} - \beta\gamma p_A\right)\\ &= \frac{E_A}{c} - \beta p_A.\end{aligned} \tag{71}$$

Suppose that photon has no mass $m_A = 0$, *i.e.*, $\frac{E_A}{c} = p_A$ and the target elec-

tron is at rest ($p_B = 0$) before the collision. We rewrite Equation (5) as

$$\beta = \frac{p_A}{\frac{E_A}{c} + m_B c} = \frac{\frac{E_A}{c}}{\frac{E_A}{c} + m_B c},$$

and substitute it into Equation (71). Thus we obtain

$$\frac{E_A'}{c} = \frac{\frac{E_A}{c}}{1 + \frac{E_A}{m_B c^2}(1 - \cos\theta)}. \tag{72}$$

This equation gives the photon energy after the collision. Hence, using the relation $E = h\nu = h\frac{c}{\lambda}$, we obtain

$$\lambda' - \lambda = \frac{h}{m_B c^2}(1 - \cos\theta), \tag{73}$$

which is the Compton wavelength shift.

3.6. In the Limit $c \to \infty$

Using the limit of Equation (36), the parameters of the ellipse become the followings:

$$\text{minor semiaxis} \quad p^* \to \frac{p_A m_B c - p_B m_A c}{\sqrt{(m_A + m_B)^2 c^2 - 2 p_A p_B}} = \frac{m_B p_A - m_A p_B}{\sqrt{(m_A + m_B)^2 - 2 p_A p_B / c^2}} \to \frac{m_B p_A - m_A p_B}{m_A + m_B}, \tag{74}$$

$$\text{major semiaxis} \quad \gamma p^* \to \frac{(m_A c + m_B c)(p_A m_B c - p_B m_A c)}{(m_A + m_B)^2 c^2 - 2 p_A p_B} = \frac{(m_A + m_B)(p_A m_B - p_B m_A)}{(m_A + m_B)^2 - 2 p_A p_B / c^2} \to \frac{m_B p_A - m_A p_B}{m_A + m_B}, \tag{75}$$

$$\text{eccentricity} \quad \beta\gamma p^* \to \frac{(p_A + p_B)(p_A m_B c - p_B m_A c)}{(m_A + m_B)^2 c^2 - 2 p_A p_B} = \frac{(p_A + p_B)(p_A m_B - p_B m_A)/c}{(m_A + m_B)^2 - 2 p_A p_B / c^2} \to 0, \tag{76}$$

$$\text{midpoint of foci} \quad \beta\gamma \frac{E_A^*}{c} \to \frac{(p_A + p_B)(m_A c m_B c - p_A p_B + m_A^2 c^2)}{(m_A + m_B)^2 c^2 - 2 p_A p_B} = \frac{(p_A + p_B)(m_A^2 + m_A m_B - p_A p_B / c^2)}{(m_A + m_B)^2 - 2 p_A p_B / c^2} \to m_A \frac{p_A + p_B}{m_A + m_B} = m_A V, \tag{77}$$

$$\begin{aligned}\text{midpoint of foci}\quad \beta\gamma\frac{E_B^*}{c} &\to \frac{\left(p_A+p_B\right)\left(m_A c m_B c - p_A p_B + m_B^2 c^2\right)}{\left(m_A+m_B\right)^2 c^2 - 2p_A p_B} \\ &= \frac{\left(p_A+p_B\right)\left(m_B^2 + m_A m_B - p_A p_B/c^2\right)}{\left(m_A+m_B\right)^2 - 2p_A p_B/c^2} \\ &\to m_B\frac{p_A+p_B}{m_A+m_B} = m_B V,\end{aligned} \tag{78}$$

where V is given by Equation (35). The minor and major semiaxes become the same and the eccentricity becomes zero. This shows that the ellipse approaches the circle, which recovers the Newtonian collision [3] [4] [7] [8].

4. Summary

We reexamined the elastic collision problems in the special relativity by using the detour through the center-of-mass system. Hopping to the center-of-mass system by the Lorentz transformation and jumping back to the laboratory system by the inverse transformation, we obtain the momenta and energies in the laboratory system after the collision without calculating any simultaneous equations which are often used in the literature. We also show that this process is applicable to the collisions both one and two dimensions in the same manner. This process makes students understand the collision problems in a unified way.

Acknowledgements

The author thanks the anonymous reviewer for his helpful suggestions.

Conflicts of Interest

The author declares no conflicts of interest regarding the publication of this paper.

References

[1] Takeuchi, T. (2010) An Illustrated Guide to Relativity. Cambridge University Press Cambridge. https://doi.org/10.1017/CBO9780511779121

[2] Ogura, A. (2017) Analyzing Collisions in Classical Mechanics Using Mass-Momentum Diagrams. *European Jounal of Physics*, **38**, Article ID: 055001. https://doi.org/10.1088/1361-6404/aa750b

[3] Landau, L.D. and Lifshitz, E.M. (1976) Mechanics. Butterworth-Heinenann, Oxford.

[4] Ogura, A. (2018) Diagrammatic Approach for Investigating Two Dimensional Elastic Collisions in Momentum Space I: Newtonian Mechanics. *World Journal of Mechanics*, **8**, 343-352. https://doi.org/10.4236/wjm.2018.89025

[5] Saletan, E.J. (1997) Minkowski Diagrams in Momentum Space. *American Journal of Physics*, **65**, 799-800. https://doi.org/10.1119/1.18651

[6] Bokor, N. (2011) Analyzing Collisions Using Minkowski Diagrams in Momentum Space. *European Journal of Physics*, **32**, 773-782. https://doi.org/10.1088/0143-0807/32/3/013

[7] Landau, L.D. and Lifshitz, E.M. (1975) The Classical Theory of Fields. Butter-

worth-Heinenann, Oxford.

[8] Ogura, A. (2018) Diagrammatic Approach for Investigating Two Dimensional Elastic Collisions in Momentum Space II: Special Relativity. *World Journal of Mechanics*, **8**, 353-361. https://doi.org/10.4236/wjm.2018.89026

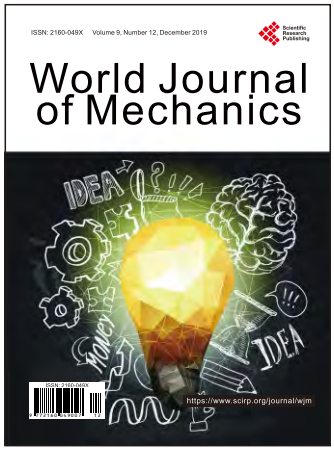

Call for Papers

World Journal of Mechanics (WJM)

ISSN 2160-049X (Print) ISSN 2160-0503 (Online)
https://www.scirp.org/journal/wjm

World Journal of Mechanics (WJM) is an international peer-reviewed journal dedicated to presenting the English original research studies, reviews in the general field of mechanics including the mechanics of solids, structures and fluids and their interaction.

Subject Coverage

This journal invites original research and review papers that address the following issues. Topics of interest include, but are not limited to:

- Applied Mathematics and Mechanics
- Biomechanics and Modeling in Mechanobiology
- Celestial Mechanics and Dynamical Astronomy
- Classical and Quantum Aspects of Mechanics
- Computational Mechanics
- Computer Methods in Applied Mechanics and Engineering
- Continuum Mechanics and Thermodynamics
- Damage Mechanics
- Dynamics and Vibration Control
- Elasticity and Plasticity
- Engineering Fracture Mechanics
- Environmental Fluid Mechanics
- Experimental Mechanics
- Fluid Mechanics and Aerodynamics
- Mathematical Fluid Mechanics
- Mathematics and Mechanics of Solids
- Mechanical Behavior of Biomedical Materials
- Mechanical Engineering Science
- Mechanical Systems and Signal Processing
- Mechanics & Astronomy
- Mechanics and Materials in Design
- Mechanics in Medicine and Biology
- Mechanics of Materials
- Mechanics of Time-Dependent Materials
- Microfluidics
- Micromechanics and Microengineering
- Multi-Scale Mechanics
- Nanomechanics
- Non-Linear Mechanics
- Non-Newtonian Fluid Mechanics
- Numerical and Analytical Methods in Geomechanics
- Probabilistic Engineering Mechanics
- Rock Mechanics and Mining Sciences
- Solid and Structural Mechanics
- Statistical Mechanics and Its Applications
- Terramechanics
- Theoretical and Applied Fracture Mechanics
- Thermophysics and Aeromechanics
- Thin Film Mechanics
- Viscoelasticity

We are also interested in short papers (letters) that clearly address a specific problem, and short survey or position papers that sketch the results or problems on a specific topic. Authors of selected short papers would be invited to write a regular paper on the same topic for future issues of World Journal of Mechanics.

Notes for Intending Authors

Submitted papers should not have been previously published nor be currently under consideration for publication elsewhere. Paper submission will be handled electronically through the website. All papers are refereed through a peer review process. For more details about the submissions, please access the website.

Website and E-Mail

https://www.scirp.org/journal/wjm E-mail: wjm@scirp.org

What is SCIRP?

Scientific Research Publishing (SCIRP) is one of the largest Open Access journal publishers. It is currently publishing more than 200 open access, online, peer-reviewed journals covering a wide range of academic disciplines. SCIRP serves the worldwide academic communities and contributes to the progress and application of science with its publication.

What is Open Access?

All original research papers published by SCIRP are made freely and permanently accessible online immediately upon publication. To be able to provide open access journals, SCIRP defrays operation costs from authors and subscription charges only for its printed version. Open access publishing allows an immediate, worldwide, barrier-free, open access to the full text of research papers, which is in the best interests of the scientific community.

- High visibility for maximum global exposure with open access publishing model
- Rigorous peer review of research papers
- Prompt faster publication with less cost
- Guaranteed targeted, multidisciplinary audience

Scientific Research Publishing

Website: https://www.scirp.org

Subscription: sub@scirp.org

Advertisement: service@scirp.org